SUPPORTING INFORMATION

Photon avalanche in lanthanide doped nanoparticles for biomedical applications: superresolution imaging

Artur Bednarkiewicz[1,2*], Emory Chan[3], Agata Kotulska[1,2],

Lukasz Marciniak[2], Katarzyna Prorok[1]

1. PORT Polish Center for Technology Development, Wroclaw, Poland
2. Institute of Low Temperature and Structure Research, Polish Academy of Sciences, Wroclaw, Poland
3. The Molecular Foundry, Lawrence Berkeley National Laboratory, Berkeley, CA 94720, USA

Emission branching ratio

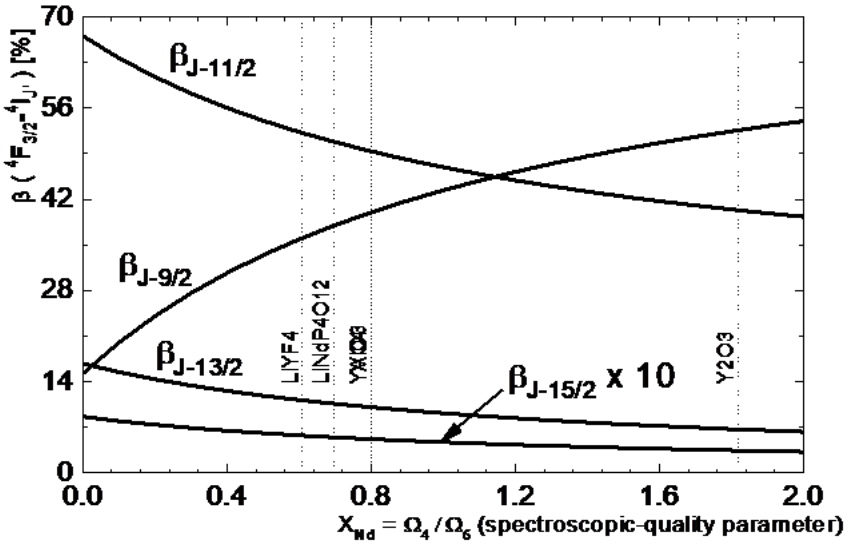

Figure S1. The theoretical emission branching ratio as a function of spectroscopic Nd parameter $X_{Nd}=\Omega_4/\Omega_6$.

Following W. Macfarlane et al.[1] one may estimate the emission branching ratio $\beta_{JJ'} = I(^4F_{3/2}\rightarrow{}^4I_{J'}) / \beta_{J'}I(^4F_{3/2}\rightarrow{}^4I_{J'})$, where J'=15/2, 13/2, 11/2, 9/2 based on Judd-Ofelt theory as

$$\beta_{JJ'}(X_{Nd}) = \frac{\left(a_{J'}\cdot X_{Nd} + b_{J'}\right)\cdot \lambda_{JJ'}^{-3}}{\sum_{J'}\left(a_{J'}\cdot X_{Nd} + b_{J'}\right)\cdot \lambda_{JJ'}^{-3}}$$

Where $a_{J'}$ and $b^{J'}$ are constants equal to the squared matrix elements of the irreducible tensor operators of rank 4 and 6

$$a_{J'} = \left|\langle\, {}^4F_{3/2} \left\| U^{(4)} \right\| {}^4I_{J'} \rangle\right|^2$$

$$b_{J'} = \left|\langle\, {}^4F_{3/2} \left\| U^{(6)} \right\| {}^4I_{J'} \rangle\right|^2$$

And the spectroscopic parameter of Nd^{3+} - X_{Nd} is defined as the ratio between phenomenological Ω_4 to Ω_6 Judd-Ofelt parameter. Figure S1 presents the emission branching ratio versus X_{Nd}, where vertical lines indicate $B_{JJ'}$ values for different hosts. The $\beta_{JJ'}$ is important in our discussion, because it determines the effectiveness, the intermediate $^4I_{11/2}$ level is populated by radiative transitions from $^4F_{3/2}$ metastable level. This in turn determines the avalanche threshold and temperature dependent $^4F_{3/2} \rightarrow {}^4I_{9/2}$ emission transients.

Sub-diffraction imaging vs non-linearity of emission center

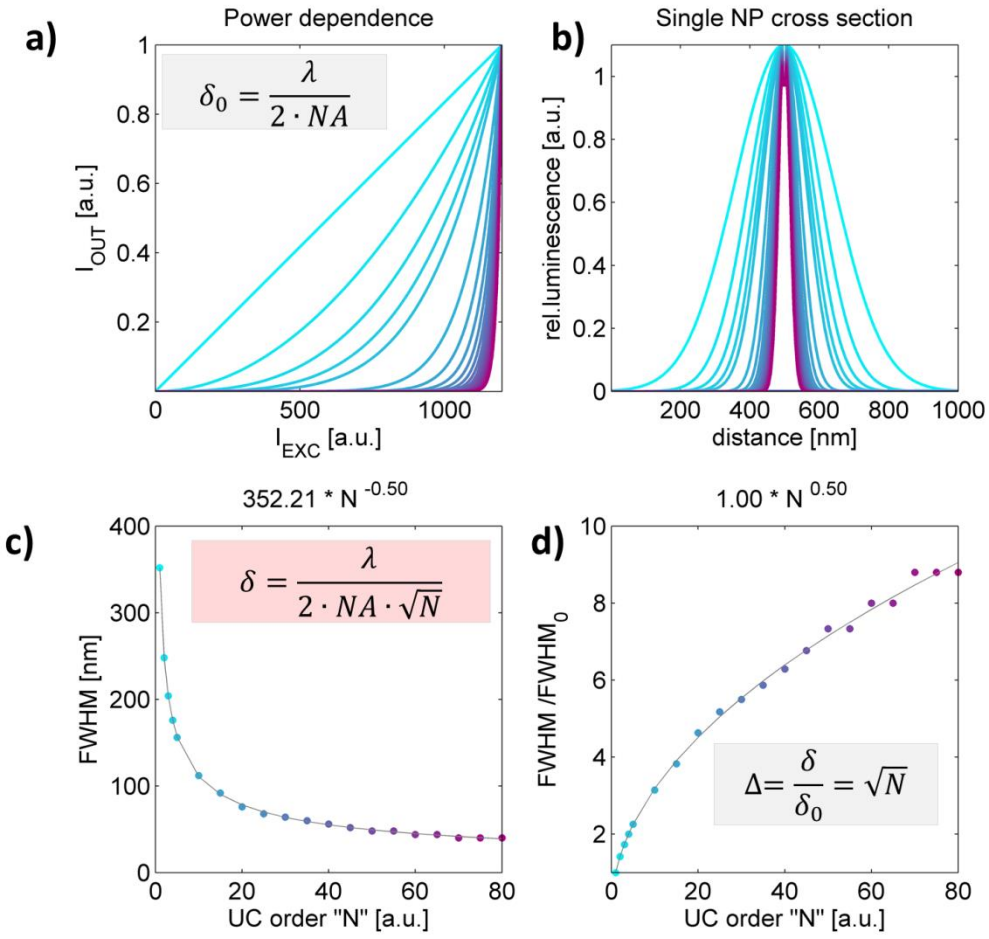

Figure S2. The role on in-out non-linearity in improving the sub-diffraction imaging *(a) the in-out non-linear relationships $I_{OUT} = (I_{EXC})^N$, for N = 1..80; the original diffraction limit is defined as $\delta_0=\lambda/(2\,NA)$; (b) the point-spread function cross-sections obtained for non-linear in-out characteristics of materials for N=1..80; (c) the full-width at half maximum obtained from data in panel (b) and fitted with $\delta_0/N^{0.5}$ equation; (d) resolution enhancement $\Delta=\delta/\delta_0=N^{0.5}$ versus the non-linear order N.*

The rate-equation model

Based on the energy levels in Nd^{3+}, we have developed a set of rate-equations, which describe the averaged behavior of the system

$$\frac{\partial n_1}{\partial t} = W_{NR}\cdot n_2 + \frac{\frac{\beta_9\cdot n_5}{2}}{\tau_{Nd}} - W_{CR}\cdot n_1\cdot n_5 - W_{AT}\cdot n_1\cdot exp\left(\frac{-\Delta E}{k\cdot T}\right) \quad \text{Eq.S1}$$

$$\frac{\partial n_2}{\partial t} = W_{NR}\cdot (n_3 - n_2) - \frac{\sigma_{1064}^{ESA}\cdot I_{EXC}}{h\nu}\cdot n_2 + \frac{\frac{\beta_{11}\cdot n_5}{2}}{\tau_{Nd}} + W_{AT}\cdot n_1\cdot exp\left(\frac{-\Delta E}{k\cdot T}\right) \quad \text{Eq.S2}$$

$$\frac{\partial n_3}{\partial t} = W_{NR}\cdot (n_4 - n_3) + \frac{\beta_{13/2}\cdot n_5}{\tau_{Nd}} \quad \text{Eq.S3}$$

$$\frac{\partial n_4}{\partial t} = 2\cdot W_{CR}\cdot n_1 n_5 - W_{NR}\cdot n_4 + \frac{\beta_{15/2}\cdot n_5}{\tau_{Nd}} \quad \text{Eq.S4}$$

$$\frac{\partial n_5}{\partial t} = \frac{\sigma_{1064}^{ESA}\cdot I_P}{h\nu}\cdot n_2 - W_{CR}\cdot n_1 n_5 - \frac{n_5}{\tau_{Nd}} \quad \text{Eq.S5}$$

$$\sum_{J'=\frac{9}{2};\frac{11}{2};\frac{13}{2};\frac{15}{2}} \beta_{J'} = 1; \quad \sum_{i=1..5} n_i = 1;$$

The equations marked by gray background, indicate thermal population of $^4I_{11/2}$ in respect to the ground $^4I_{9/2}$ level. Because these rate equations can be solved analytically only for low excitation regime, we have decided to solve them numerically. The following phenomenological parameters have been set:

1. rate of non-radiative transitions ($W_{NR}=1/10^{-5}$ s^{-1}) – this parameter is characteristic for a given host material
2. rate of cross-relaxation ($W_{CR}=1/10^{-5}$ s^{-1}) – this parameter is proportional to the concentration of Nd^{3+} ions

3. variable intensity of photoexcitation (I_{EXC} from … to ….), where the pumping rate is defined by the absorption cross section $\sigma_{1064}^{ESA}$and pumping intensity I_P at hν=1064 nm and.
4. photoexcitation pulse width (s) – setting reasonably long photoexcitation pulse, enables to find the steady-state intensity
5. energy gap ($\Delta E = 1900\ cm^{-1}$) – this energy gap is energy difference between highest Stark level of the ground $^4I_{9/2}$ state and lowest stark level of the $^4I_{11/2}$ level.
6. All in silico experiments were performed at 42 ^oC. Grey part of the equations correspond to thermal initial population of the first $^4I_{11/2}$ excited state, which shall contribute to photon avalanche threshold

All other parameters have their typical meaning: h-Planck constant, k=Boltzmann factor, $\beta_{J'}$ (J'=9/2,11/2,13/2,15/2) are branching ratios (see below). First, the transients were calculated for n_1 to n_5 levels. To evaluate steady-state emission intensity, the photoexcitation pulse was fixed long enough to get saturation (Fig.S3, I_{SS}) in transient of the population n_5, i.e. $I(t) \sim n_5 = fun(I_{EXC}, W_{NR}, W_{CR}, \Delta E, T, t_{PULSE}, t)$. In a similar way the half-rise times were calculated $I(t_{1/2}) = ½ \cdot I_{SS}$. The variability of these factors were subsequently presented as a function of excitation intensity (I_P), non-radiative ($1/W_{NR}$) and cross-relaxation ($1/W_{CR}$) rates.

Table S1. Energies of Z_5 ($^4I_{9/2}$) and Y_1 ($^4I_{11/2}$) Stark levels of Nd^{3+} ions and energy differences between Z1 and Y_1 (ΔE) and between Z_5 and Y_1 (ΔE_{min}) Stark levels of different host materials

Host material	**Z_5**	**Y_1**	**ΔE_{min}**	**ΔE**	**Ref**
$Y_3Al_5O_{12}$	848	2001	1153	2001	[9]
Y_2O_3	640	1899	1259	1899	[2]
Gd_2O_3	610	1900	1290	1900	
$YGdO_3$	580	1910	1330	1910	
$YAlO_3$ (YAP)	671	2023	1352	2023	
$LiLaP_4O_{12}$	326	1939	1613	1939	[3]

Based on Judd-Ofelt theory the Einstein coefficient (radiative rates) is proportional to line strength of electric dipole transition, which is expressed as:

$$A_{ij} \sim s_{JJ'}^{ed} \sum_{\lambda=2,4,6} \Omega_\lambda \cdot \left| \langle 4f^N \alpha[SL]J \| U^{(\lambda)} \| 4f^N \alpha'[S'L']J' \rangle \right|^2$$

The $<||U^{(\lambda)}||>$ is reduced matrix elements of the irreducible tensor operators, which indicates theoretical probability of transition between SLJ and S'L'J manifolds and the [Ω_2 Ω_4 Ω_6] are intensity parameters characteristic for given ione in given matrix. Taking into account the [Ω_2 Ω_4 Ω_6] = [6.07 3.05 10.52] Judd-Ofelt parameters for e.g. fluorides as well as reduced tensor [U_2 U_4 U_6] = [0.001 0.2371 0.3972] for $^4I_{9/2} \rightarrow {}^4F_{5/2}$ at ~800 nm (which is typically used to pump Nd based lasers), and [U_2 U_4 U_6] = [0.0000 0.1136 0.4104] for $^4I_{11/2} \rightarrow {}^4F_{3/2}$ at ~1064 nm (which is typically used as laser emission), one may calculate $s^{ed}_{4I9/2 \rightarrow 4F5/2}$ (800nm)= $4{,}907769 \cdot 10^{-20}$ cm^2, while $s^{ed}_{4I11/2 \rightarrow 4F3/2}$ (1064nm) = $4{,}663888 \cdot 10^{-20}$ cm^2, which means, the integrated absorption cross section of ESA should be around 95% of GSA, if only the $^4I_{11/2}$ level is fully populated. The latter σ was actually measured to be $10.75 \cdot 10^{-20}$ cm^2 in Nd^{3+} doped $NaYF_4$ single crystals[4]. Based on E.S. Levy et al. estimations and the modeling performed there for Nd^{3+} ions, the $\sigma_{4I9/2 \rightarrow 4F3/2}$ (1064nm) ~$1 \cdot 10^{-25}$ cm^{-2}. Therefore the A_{GSA}/A_{ESA} ratio equals to $\sigma_{4I9/2 \rightarrow 4F3/2}$ (1064nm) / $\sigma_{4I11/2 \rightarrow 4F3/2}$ (1064nm) ~ $1 \cdot 10^{-25}$ cm^{-2} / $95\% \cdot 10.75 \cdot 10^{-20}$ cm^2 = $0.098 \cdot 10^{-5}$ = $0.98 \cdot 10^{-4}$, which satisfy the condition $R<10^{-4}$ and thus should classify the process as photon avalanche[5,6]. It is important to mention, the Nd doped $NaYF_4$ single crystals exhibited 26%, 100% and 389% higher absorption cross section and 54%, 147% and 231 % higher emission cross section than Nd^{3+} doped YAG, YLF, BYF. [4] This is also in agreement with calculations made by Joubert et al[7]. The only studies on PA in Nd^{3+} ions demonstrated 4g13 nm PA emission under 603.6 nm in $LiYF_4$ single crystal, at temperatures <40K with lasing slope factor efficiency up to 11%. The critical parameter R has reached $1.7 \cdot 10^{-4}$ for avalanche at T 40 K[1,7].

Not too much information can be found on non-radiative rates, which in fact determine the balance between non-radiative losses and looping, which is a fundamental requirement for PA to occur. In Nd^{3+}, the energy gap between $^4I_{15/2}$, $^4I_{13/2}$ and $^4I_{11/2}$ and the ground $^4I_{9/2}$ state are equal to around 1540, 1700 and 1480 cm^{-1} respectively, with W_{NR} ~10^3-10^4 s^{-1} (based on LaF_3 host[8]). Such W_{NR} corresponds to A_{NR} ~ 10^{-3}-10^{-4} s, which, according to Fig.S3 makes the presented system closer to looping rather than PA. The W_{NR} has a tremendous impact on the PA behaviour in Nd^{3+} (as shown in Fig.3e,f), because this mechanism is present and necessary both to get looping, and simultaneously deplete the $^4I_{11/2}$ level. However, based on data available in the literature and the energy gap law, it is impossible to get univocal and reliable values for other hosts such as $NaYF_4$ (see discussion in chapter 4.2 of Kaminski). We have therefore presented the performance of the studied PA system for variable W_{NR} values.

The impact of host material parameters on the PA behavior

It is necessary to find a material, which through a proper balance between CR and NR processes enhances PA and enables to get very high orders of PA reaching > 50. As one may see from Fig.3, lower CR rates (lower Nd^{3+} concentrations) enhances PA effect, while increasing A_{CR} leads to more looping like behavior, and in consequence to lower N and higher PA threshold. Higher NR rates significantly reduces PA threshold, change PA into looping.

Since the power dependent in-out process is described by allometric relationship

$$P_{OUT}(P_{IN}) = a \cdot (P_{IN})^N$$

To simplify and speed up the analysis, both sides of the equation can be recalculated with a logarithmic function, which gives

$$\ln(P_{OUT}) = \ln[a \cdot (P_{IN})^N]$$

$$\ln(P_{OUT}) = \ln(a) + N ln(P_{IN})$$

thus substituting

$$P'_{OUT} = \ln(P_{OUT}) ; a' = \ln(a); P'_{IN} = ln(P_{IN})$$

one gets a linear function $P'_{OUT} = a' + N \cdot P'_{IN}$, which can be easily fitted with 1-order polynominal. This procedure was implemented in a matlab code presented below, which enabled, based on W_{CR} and W_{NR} dependent in-out curves, to calculate power dependent non-linearities $N(P_{IN})$, as presented in Fig.3d and f, respectively. Such 'adaptive' approach is required because of variable and steep changes of the photon avalanche in-out relationships make the evaluation of N susceptible to the manual selection of the range on the in-out curve.

```
function TableN = CalculateTableN( PowerDepTable)

TableX = log(PowerDepTable(:, 1)); % Excitation intensity
TableY = log(PowerDepTable(:, 2)); % Emission itensity

SizeT = max(size(TableX));
SD = 0;                 % standard deviation
SDErr = 0.02;           % acceptable SD
MinimalCheck = 20;      % start fitting with at least 10 data points

PowerNTable = zeros(SizeT-10,2);    % define table for power dependent N

for idxT=1:SizeT-MinimalCheck       % go through all (but last MinimalCheck) data points
```

```
    Didx = MinimalCheck;
    SD = 0;
    % as long as dataset is nicely fitted with p1 * X^N + p2
    % enlanrge the dataset beyond MinimalCheck datapoints
    while (SD < SDErr) & (idxT + Didx < SizeT)
        % extract Didx datapoint for fitting
        TableX2 = TableX( idxT: idxT + Didx) - TableX( idxT);
        TableY2 = TableY( idxT: idxT + Didx);
        % fit the dataset with p1 * X^N + p2

        [p,ErrorEst] = polyfit(TableX2,TableY2,1);
        % generate fitted curve
        [f, delta] = polyval(p,TableX2, ErrorEst);
        % calculate SD based on residuals
        SD = sum((delta.^2)./(f.^2));
        % build the result table using original X and power factor N
        PowerNTable(idxT,1) = PowerDepTable(idxT, 1);
        PowerNTable(idxT,2) = p(1);
        Didx = Didx + 1;
    end;
end;

%       plot(TableX2, TableY2,'o', TableX2, f, '-'); hold on;

TableN = PowerNTable;
clc;
sprintf('Progress of analysis %3.1f %% ', [100*idxT / (SizeT-MinimalCheck)])
end;
```

The impact of excitation and materials properties of spatial resolution of PASSI

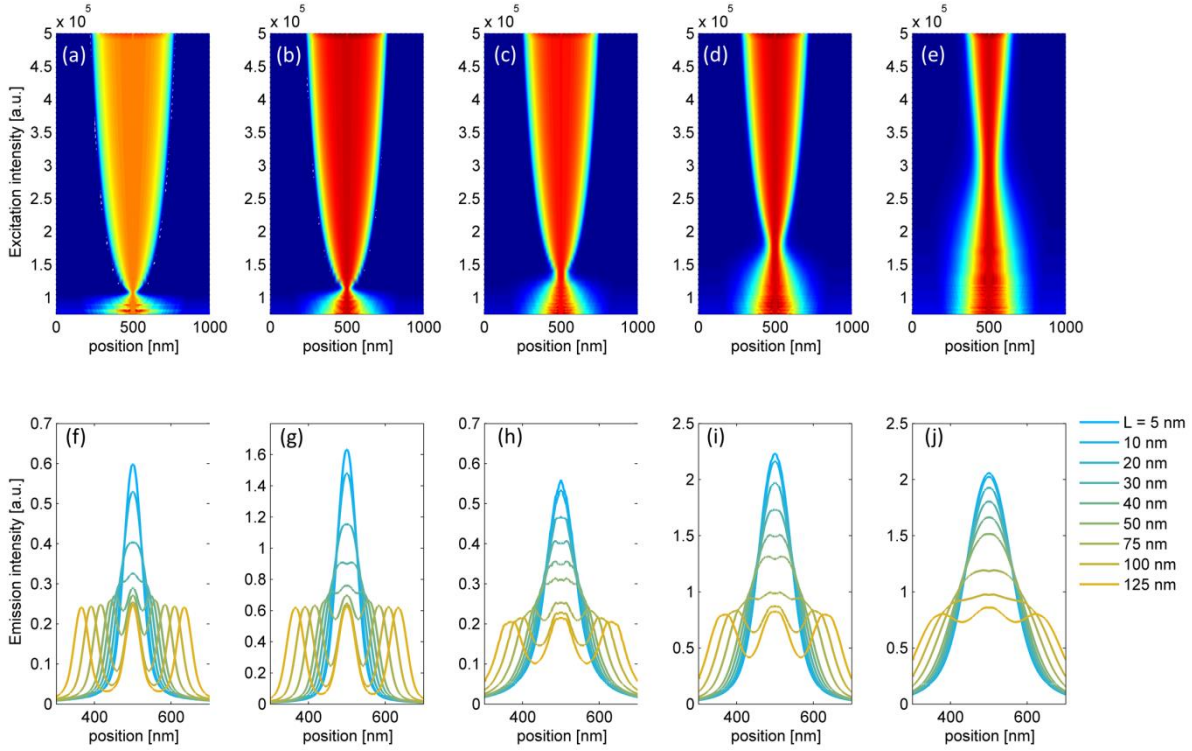

Figure S3. Resolution versus cross-relaxation rate and excitation intensity. Top row presents the excitation intensity (y axis) dependent profile measured in silico for single 10 nm PA NP at looping strength (A_{CR}=1,2,5,10,20 e-5 s^{-1}) at subsequent columns (these data served to obtain the Fig.2e data). Bottom row presents (similar to Fig.2b,g) the cross section of 3 PA NPs (10nm in diameter) displaced (by 5,10,20,30,40,50,75,100 and 125 nm) for different looping strength (A_{CR}=1,2,5,10,20 e-5 s^{-1}) at subsequent columns and at the optimum I_0=1.07e5, 1.15e5, 1.3e5, 1.8e5, 3.0e5 excitation intensities, which were adjusted to respective A_{CR}.

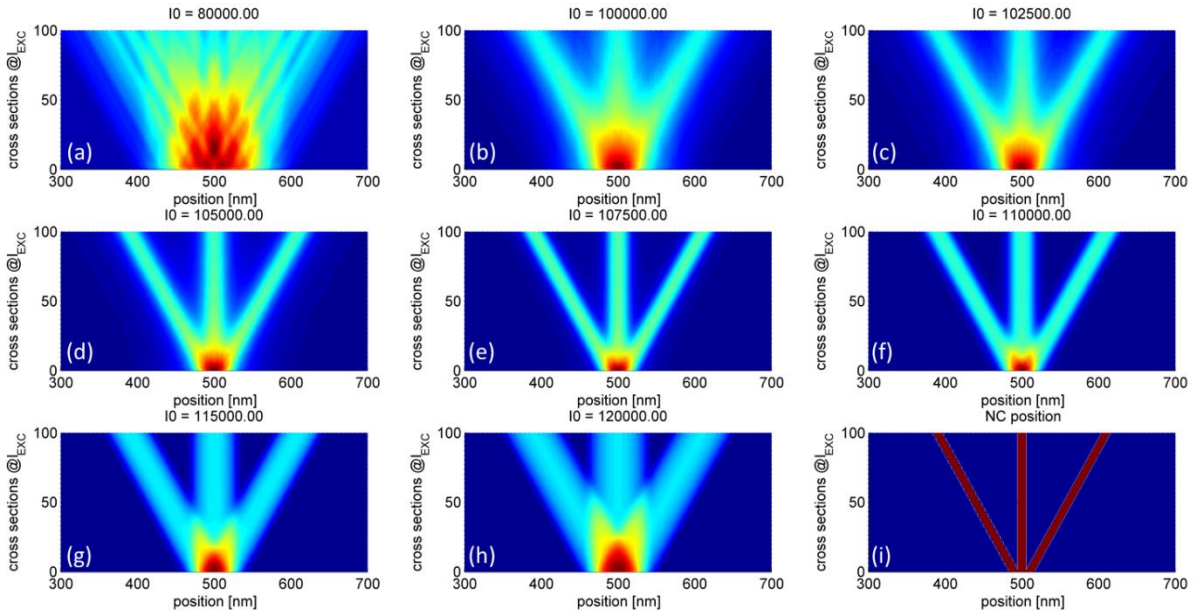

Figure S4. The impact of excitation intensity on the spatial resolution. Cross sections of the 3 NP phantom (i) versus distance between NPs (along y axis) and for different I_o excitation intensity (a-h).

Lateral optical resolution of PASSI

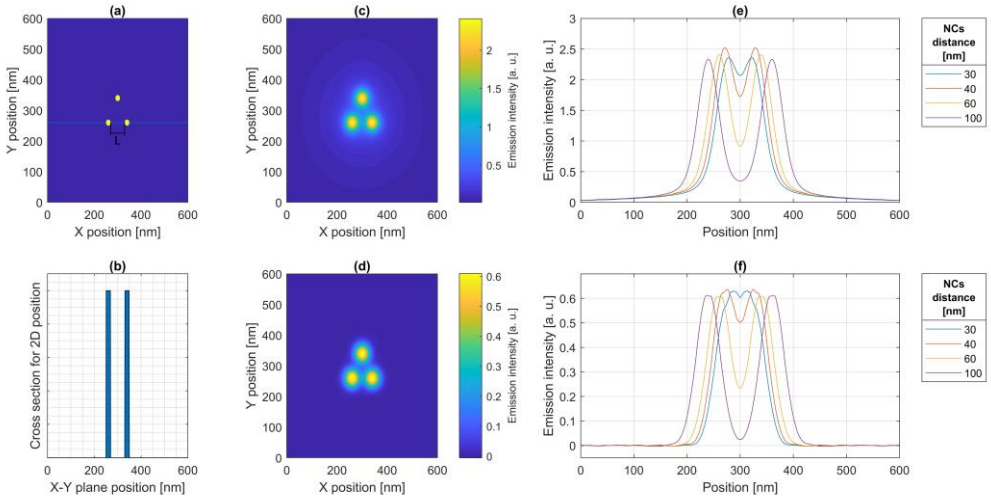

Figure S5. ***Spatial resolution enhancement using photon avalanche labels.*** *(a) Phantoms composed of 3 NPs (ϕ=20 nm PA NPs) placed at L = 60 nm distances are reconstructed using optimal PA conditions, and (b) respective cross sections of graph for distance L = 60 nm along a light blue line. Phantom composed of 20 nm PA NPs (distance L = 60 nm) reconstructed with (c) steady state avalanche and (d) time-gated avalanche models. (e) Emission intensity cross section obtained along the line showed in graph (a) was reconstructed with (e) steady state avalanche and (f) time-gated avalanche models, respectively for L = 30, 40, 60 and 100 nm.*

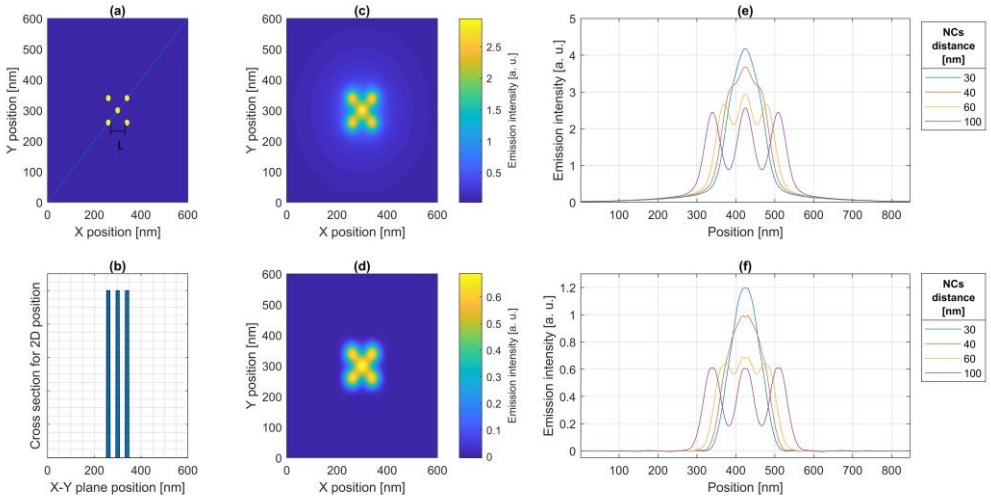

Figure S6. ***Spatial resolution enhancement using photon avalanche labels.*** *(a) Phantoms composed of 5 NPs (ϕ=20 nm PA NPs) placed at L = 60 nm distances are reconstructed using optimal PA conditions, and (b) respective cross sections of graph for distance L = 60 nm along a light blue line. Phantom composed of 20 nm PA NPs (distance L = 60 nm) reconstructed with (c) steady state avalanche and (d) time-gated avalanche models. (e)*

Emission intensity cross section obtained along line showed in graph (a) and reconstructed with (e) steady state avalanche and (f) time-gated avalanche models, respectively for L = 30, 40, 60 and 100 nm.

Axial optical resolution of PASSI

For a Gaussian-profile beam, the 1/e beam radius is given by [9]:

$$w(z) = w_0 \cdot [1 + (z/z_R)^2]^{1/2} \qquad \text{Eq.1.}$$

Where $w_0 = \lambda/NA \cdot \pi$ (Eq.2) is the spot size at the focus at z=0, and $z_R = w_0/NA$ is Raleigh length. The pump intensity is expressed as [9]:

$$I_p(x,y,z) = I_0 \cdot [w_0/w(z)]^2 \cdot exp\left(-\frac{(x^2+y^2)}{w^2(z)}\right) \cdot exp(-\varepsilon \cdot z) \qquad \text{Eq.3}$$

where ε is an attenuation coefficient of the pump beam in the sample. Let's assume small attenuation coefficient of the sample for pump beam (ε=0.001), λ=1064, NA=1.4. This enables to visualize the beam cross section.

According to the ref.[10], diffraction for super-resolution localization of single molecule is defined as $\delta_0/(N^{-0.5})$, where δ_0 is width of the diffraction-limited point spread function and N number of detected photons.

The intensity of conventional (liner, Stokes) fluorescence excited by Gaussian beam (ZX plane) is presented in Figure S7a and b based on the above equations. The luminescence of non-linear fluorophore is presented in Fig.S7 at panels c and d (for N=2), e and f (for N=10), g and h (for N=30) and i and j (for N=60).

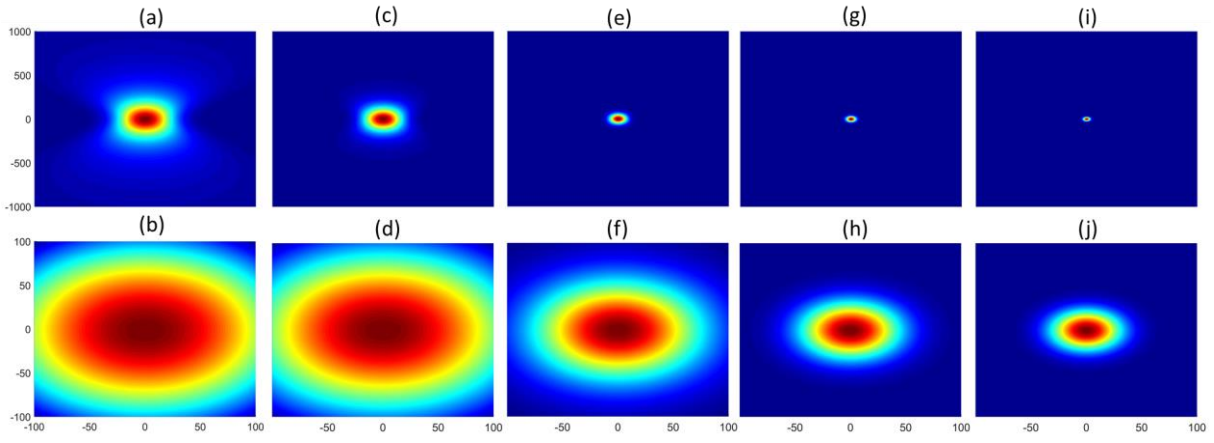

Figure S7: *Linear axial (along z axis) intensity for Gauss profile of laser beam (a), (b). Intensities of emission from N^{th} order non-linear processes, respectively for N=2 (c,d), 10 (e,f), 30 (i,j) and 60 (g,h).*

Supporting information references

1. Macfarlane, R. M. Inhomogeneous broadening of spectral lines in doped insulators. *J. Lumin.* **45**, 1–5 (1990).

2. Nash, K. L., Dennis, R. C., Ray, N. J., Gruber, J. B. & Sardar, D. K. Absorption intensities, emission cross sections, and crystal field analysis of selected intermanifold transitions of Ho3+ in Ho3+:Y2O3 nanocrystals. *J. Appl. Phys.* **106**, 63117 (2009).

3. Marciniak, Ł., Bednarkiewicz, A., Hreniak, D. & Strek, W. The influence of Nd^{3+} concentration and alkali ions on the sensitivity of non-contact temperature measurements in $ALaP_4O_{12}:Nd^{3+}$ (A = Li, K, Na, Rb) nanocrystalline luminescent thermometers. *J. Mater. Chem. C* **4**, 11284–11290 (2016).

4. Peterson, R. & Cassanho, A. Evaluation of Nd:NYF as a new laser material. in *Advanced Solid-State Lasers* TuB7 (Optical Society of America, 2001). doi:10.1364/ASSL.2001.TuB7

5. Seto, D. *et al.* Nanoscale optical thermometry using a time-correlated single-photon counting in an illumination-collection mode. *Appl. Phys. Lett.* **110**, (2017).

6. Joubert, M.-F. Photon avalanche upconversion in rare earth laser materials. *Opt. Mater. (Amst).* **11**, 181–203 (1999).

7. Joubert, M. F., Guy, S. & Jacquier, B. Model of the photon-avalanche effect. *Phys. Rev. B* **48**, 10031–10037 (1993).

8. E., P. Y. & A., K. A. Nonradiative Transitions of the Trivalent Lanthanides in Insulating Laser Crystals. *Phys. status solidi* **132**, 11–40 (2018).

9. Cho, S., Humar, M., Martino, N. & Yun, S. H. Laser Particle Stimulated Emission Microscopy. *Phys. Rev. Lett.* **117**, 1–5 (2016).

10. Huang, B., Babcock, H. & Zhuang, X. Leading Edge Primer Breaking the Diffraction Barrier: Super-Resolution Imaging of Cells. *Cell* **143**, 1047–1058 (2010).